All-rf-based coarse-tuning algorithm for quantum devices using machine learning

Barnaby van Straaten,[1,*] Federico Fedele,[1,*] Florian Vigneau,[1] Joseph Hickie,[1] Daniel Jirovec,[2] Andrea Ballabio,[3] Daniel Chrastina,[3] Giovanni Isella,[3] Georgios Katsaros,[2] and Natalia Ares[4,†]

[1] *Department of Materials, University of Oxford, Oxford OX1 3PH, United Kingdom*
[2] *Institute of Science and Technology Austria, Am Campus 1, 3400 Klosterneuburg, Austria*
[3] *L-NESS, Physics Department, Politecnico di Milano, via Anzani 42, 22100 Como, Italy*
[4] *Department of Engineering Science, University of Oxford, Oxford OX1 3PJ, United Kingdom*

(Received 26 September 2024; revised 23 June 2025; accepted 26 September 2025; published 10 November 2025)

Radio-frequency measurements could satisfy DiVincenzo's readout criterion in future large-scale solid-state quantum processors, as they allow for high bandwidths and frequency multiplexing. However, the scalability potential of this readout technique can only be leveraged if quantum device tuning is performed using exclusively radio-frequency measurements, that is, without resorting to current measurements. We demonstrate an algorithm that performs automatic coarse tuning of double quantum dots with only radio-frequency measurements by exploiting their bandwidth and impedance matching. The tuning was completed within a few minutes with minimal prior knowledge about the device. Our results show that it is possible to eliminate the need for transport measurements for quantum-dot tuning, paving the way for more scalable device architectures.

DOI: 10.1103/v11m-dbhm

I. INTRODUCTION

Radio-frequency (rf) reflectometry allows for high-bandwidth measurements of quantum devices [1]. Due to their potential for scalability, rf techniques play an increasingly important role in developing quantum device circuits. A recent achievement has been the high-fidelity single-shot readout of spins [2–4]. However, until now, much slower current measurements were still necessary to automatically tune quantum devices to their operating regime [5–8], even though rf measurements are sufficient [9]. This was a limiting factor for scalability because current measurements are incompatible with scalable device architectures [10–13] and are too slow for error correction [14]. The recent integration of CMOS dynamic random-access and multiplexing architectures further highlights the potential of rf reflectometry for scalable readout in quantum devices [15–18].

We demonstrate an algorithm that tunes a quantum device using rf measurements exclusively, eliminating the need to measure currents through the device. This approach relaxes the need for transport measurements and may enable new, more scalable device architectures designed to operate with rf measurements alone. The algorithm defined double quantum dots, a cornerstone of the solid-state qubit effort, which can encode either a singlet-triple qubit or a pair of Loss-DiVincenzo spin qubits [19,20].

Our algorithm exploits the bandwidth of rf measurements to acquire high-resolution two-dimensional charge stability diagrams within milliseconds [21,22]. The device's gate voltage space is efficiently explored using Gaussian processes, principal component analysis to perform blind signal separation [23–25], and Kolmogorov-Smirnov statistical tests [26], along with our fast scans. Quantum-dot features are identified using a score function based on the Fourier transform of the charge stability diagram.

We demonstrate our tuning algorithm in a hole-based quantum-dot array hosted in a Ge/SiGe heterostructure. Ge hole spin qubits are currently enjoying intense research interest owing to their ease of operation and compatibility with existing Si technology [27]. From 2018, and within just four years, a Loss-DiVincenzo qubit [28], a single-triplet qubit [29], two-qubit devices [30], and a four-qubit Ge quantum processor [31] have been realized, demonstrating the potential of Ge for quantum information. Furthermore, Ge has also hosted record-breaking ultrafast control frequencies, with Rabi frequencies exceeding 500 MHz [32].

[*] These authors contributed equally.
[†] Contact author: natalia.ares@eng.ox.ac.uk

Our algorithm contributes significantly toward scalable readout, an essential step in realizing the scalability potential of Si-compatible quantum circuits.

II. METHODS

A. The device and rf readout

We demonstrate our algorithm in a Ge/SiGe depletion-mode quantum-dot array operated as two double-dot devices, labeled A and B, where five voltage gates shaped the electrostatic potential [Fig. 1(a)]. The fabrication process of this device is similar to that described in [29]. Through bias-tees, ac and dc signals were applied to the plunger gates for each quantum dot, V_2, V_4, and V_6. A constant voltage of 2 V was set to the splitter gates V_{SL} and V_{SR} to isolate the triple-dot array from a charge sensor, which was not used for this work. Measurements were performed at 50 mK.

A device ohmic was connected to an L-matching network for rf readout. This L-matching network was formed by a 92-pF decoupling capacitor, a 2.2-μH inductor, and the parasitic capacitance to the ground of the printed circuit board and the device, C_P [Fig. 1(a)] [33]. These values were chosen to approximately match the impedance of the double-quantum-dot device [1]. With this choice of components, our rf measurements are sensitive in the region of gate voltage space where the quantum dots were in the few-hole regime. The power of the rf drive at the device was fixed at −90 dBm. The rf signal's in-phase and out-of-phase components were acquired with homodyne demodulation.

The device measurements consisted of fast two-dimensional gate voltage scans performed along specific directions in gate voltage space identified by linear combinations of gates V_{1-5} for device configuration A and V_{3-7} for configuration B (see Sec. II B for further details). To perform the fast scans, plunger gates were swept in a raster pattern using an arbitrary waveform generator [Fig. 1(b)]. These scans had an amplitude and resolution of 100 by 100 mV and 100 by 100 pixels, respectively. An integration time of 1 μs per pixel was used, enabling an entire scan to be completed in 10 ms. It was necessary to precompensate the waveforms responsible for the raster pattern for the distortion introduced by the bias tees [34]; see Appendix C.

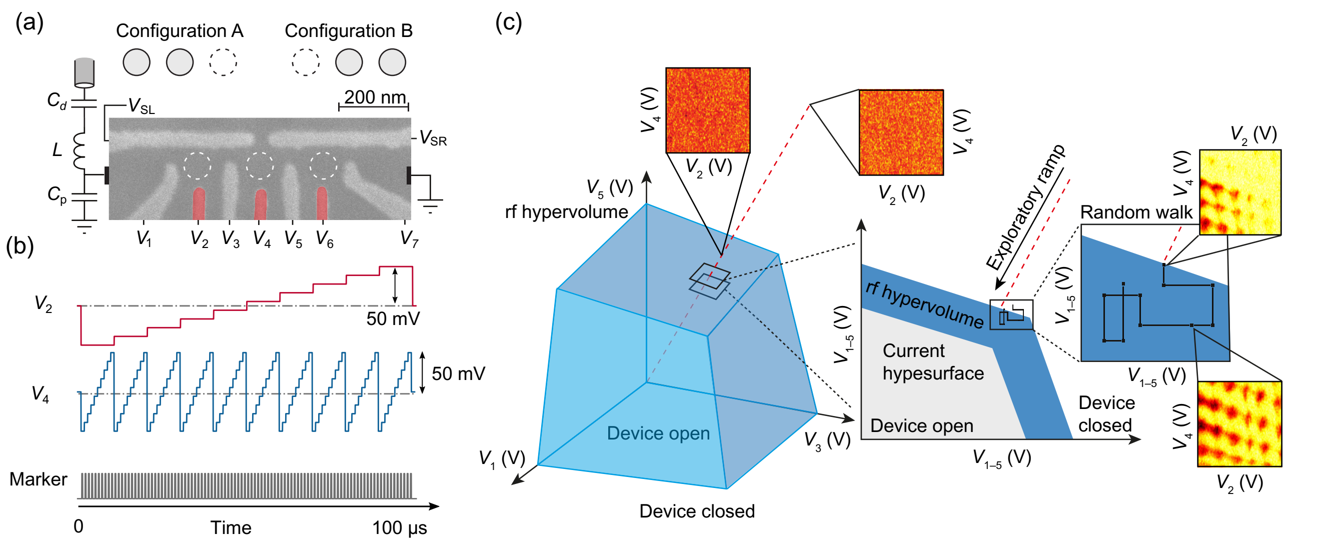

FIG. 1. (a) A scanning electron micrograph of the Ge/SiGe quantum-dot array, with an L-matching circuit connected to the device ohmic. Bias-tees are used on gates shaded in red to apply both ac and dc voltages. Devices A and B demonstrate how two different double dots can be defined in the array. (b) A diagram showing the waveforms sent to gates V_2 (V_4) and V_4 (V_6) to perform a fast two-dimensional scan of 10 × 10 pixels and 100 × 100 mV on configuration A (B), with the associated marker to trigger measurement acquisition. (c) An illustrative diagram showing an early iteration of the algorithm. For clarity, we show a simplified three-dimensional representation of the device parameter space defined by gate voltages $V_{1,3,5}$. Firstly, the algorithm performs an exploratory ramp along a randomly chosen direction, where a Gaussian process chooses the starting gate voltage coordinate to lie as close to, but still outside of, the rf hypervolume as its confidence allows. The exploratory ramp is defined using gates V_{1-5} for configuration A and V_{3-7} for B. Along the ramp, fast 2D scans are performed using gates V_2 and V_4 for A, and V_4 and V_6 for B. The rf classifier evaluates these scans to determine whether they show rf features or just noise. The first instance of the rf classifier classifying features marks the point where the exploratory ramp enters the rf hypervolume and the rf becomes sensitive. At this point, the exploratory ramp is terminated and the algorithm explores the local gate voltage region by random walk, again while taking 2D scans. The score function evaluates these scans to determine the quality of the double-dot features the algorithm has found.

B. The algorithm

Our rf coarse tuning algorithm was built from two components: a strategy to navigate through the device's gate voltage space and a score function to quantify the quality of any double-dot features found.

Previous strategies to navigate gate voltage spaces cannot be trivially applied to rf measurements, as matching networks are only sensitive over a small window of device impedances. These strategies used current measurement to search for the current hypersurface, which marks the transition between the device being "open" and "closed" [5,35]. Quantum-dot features are found near this current hypersurface.

To circumvent this limitation, we formulate an rf hypervolume to navigate by. This volume is defined as where the rf matching network is sensitive to the changes in quantum device impedance. Outside the rf hypervolume, the matching network is not sensitive, and the signal in the demodulated in-phase and out-phase components falls below the noise floor. The current hypersurface and the rf hypervolume do not necessarily intersect, and we can control the position in the gate voltage space of the rf hypervolume by choice of the matching network components. With our components, quantum-dot features were near the rf hypervolume.

Our algorithm navigates to the rf hypervolume using exploratory gate voltage ramps. These ramps slowly (at approximately $1\,\mathrm{V\,s^{-1}}$) move gate voltages toward 0 V along a randomly chosen radial direction in the space defined by voltage gates $V_1 - V_5$ for configuration A, or $V_3 - V_7$ for configuration B [Fig. 1(c)]. The first of these ramps starts from gate voltage coordinates bounded by the gate voltage upper limits, which was 4V for all gates [Fig. 2(a)]. This gate voltage limit was chosen to allow for the maximum operational range, within which the device was safe from leakage. Along the length of a ramp, the algorithm performs fast two-dimensional (2D) gate voltage scans (described in Sec. II A) every 50 mV. The algorithm evaluates each scan using a classifier to determine whether the scan shows only noise. When the ramp crosses into the rf hypervolume, the classifier will cease to detect noise, and the ramp is terminated.

The algorithm then searches for double-dot features near the gate voltages where the rf hypervolume was found using a random walk. Double-dot features are identified and quantified using a score function based on the discrete-time 2D Fourier transform (described in Sec. II B 3). The random walk is performed by perturbing a randomly chosen gate voltage by an amount sampled from a Gaussian distribution with a standard deviation of 10 mV.

The algorithm efficiently explores the gate voltage space by repeatedly undertaking these exploratory ramps. With each ramp, it might find new double-dot features that score better than any previous dot features. Over time, with repeated exploratory ramps, the algorithm explores

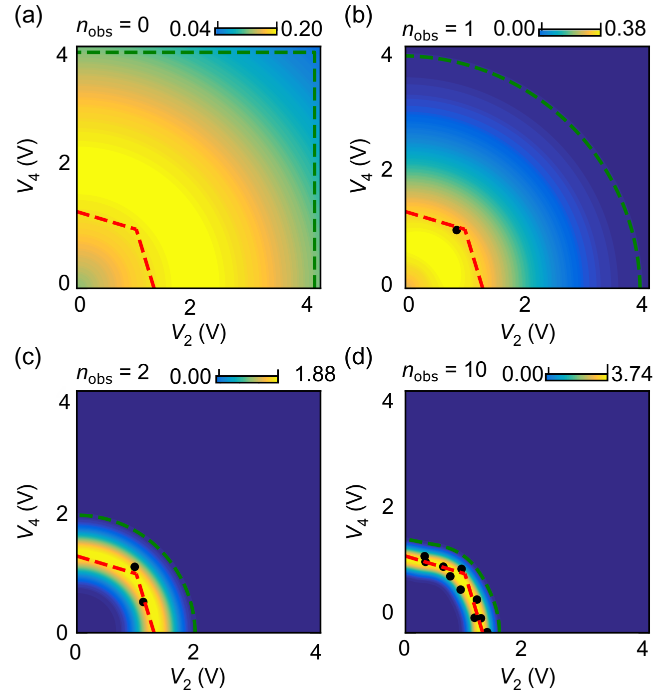

FIG. 2. (a)–(d) A series of plots illustrating the evolution of the Gaussian posterior probability distribution as it models the outer boundary of the rf hypervolume, with $n_{\mathrm{obs}} = 0, 1, 2, 10$ noisy observations of the location of the hypervolume, respectively. The color map indicates the probability density of the Gaussian posterior distribution for the location of the rf hypervolume's outside edge. The exact position of the rf hypervolume is marked in red. The noisy observations are depicted as black dots. The exploratory ramp's starting radii, at three standard deviations outside the mean, are plotted as a dashed green line.

an increasing fraction of gate voltage space; therefore, the score associated with the highest-scoring double-dot features should improve over the algorithm's run time. Concurrently, each ramp's termination gate voltage coordinate updates a Gaussian process. These observations of the hypervolume location inform the starting gate voltage coordinate of subsequent ramps, allowing them to start closer to the hypervolume and waste less time measuring regions of gate voltage space where only noise can be observed (Fig. 2). Therefore, as the algorithm improves its model for the location of the hypervolume, it becomes more efficient at exploring the gate voltage space.

The following sections describe the Gaussian process (GP), the rf classifier, and the score function used by the algorithm.

1. The Gaussian process

Our tuning algorithm utilizes a GP to estimate the radius of the outermost boundary of the rf hypervolume along a specified direction, denoted by the unit vector $\hat{x}$. GPs are particularly efficient for this task, having demonstrated robustness against different noise characteristics and device architectures [35]. The GP interpolates historical observations of the hypersurface $\mathbf{X}$ (representing gate voltage directions) and $\mathbf{R}$ (representing corresponding radius measurements) to produce a posterior Gaussian distribution encoding its belief of the location of the hypersurface in direction $\hat{x}$, such that

$$\mu(\hat{x}), \sigma(\hat{x}) = \mathcal{GP}(\hat{x}; \mathbf{X}, \mathbf{R} \mid \text{mean}_{\vec{\theta}}, \text{kernel}_{\vec{\phi}}), \qquad (1)$$

where $\mu(\hat{x})$ and $\sigma(\hat{x})$ represent the mean and standard deviation of this Gaussian. The mean function, $\text{mean}_{\vec{\theta}}$, and the kernel function, $\text{kernel}_{\vec{\phi}}$, together with their defining hyperparameters, allow the GP to interpolate observations of the hypersurface's location.

Initially, we configure the mean function to set $\mu(\hat{x})$ to the midpoint of the voltage range and the kernel function to encompass the entire voltage range within three standard deviations [Fig. 2(a)]. This initial configuration reflects our initial uncertainty about the location of the hypersurface.

As the algorithm progresses, each new observation of the rf hypersurface's location updates the GP, refining the posterior distribution [Figs. 2(b)–2(d)]. This continuous update process enables the algorithm to make increasingly accurate predictions regarding the hypersurface's boundary, thereby enhancing the efficiency of the exploratory ramps. These exploratory ramps are initiated three standard deviations outside the rf hypersurface. Between these exploratory ramps, we optimize the hyperparameters in the mean and covariance functions $(\vec{\theta}, \vec{\phi})$.

We used a constant value mean function and a scaled radial basis function plus white noise for our Gaussian processes kernel, as implemented by SCIKIT-LEARN [36].

2. The rf classifier

The role of the rf classifier is to evaluate whether one of our fast 2D scans shows noise or quantum-dot features. If a scan at a given gate voltage coordinate shows quantum-dot features, that coordinate must lie within the rf hypervolume. However, both in-phase (I) and out-of-phase (Q) components of the rf signal could contain useful information about these features [Fig. 3(a)]. Therefore, we perform blind signal separation to extract any information-bearing signal from the quadratures. We then perform a hypothesis test to see whether the extracted signal differs from noise.

To extract any signal from the quadratures, we use the popular method of principal component analysis (PCA). PCA considers the signal's covariance matrix to optimally find the direction in the IQ-plane with the largest variance and projects the data onto it [37]. Our algorithm uses PCA to optimally project a pair of 2D scans measured in both quadratures into a main one [Fig. 3(b)].

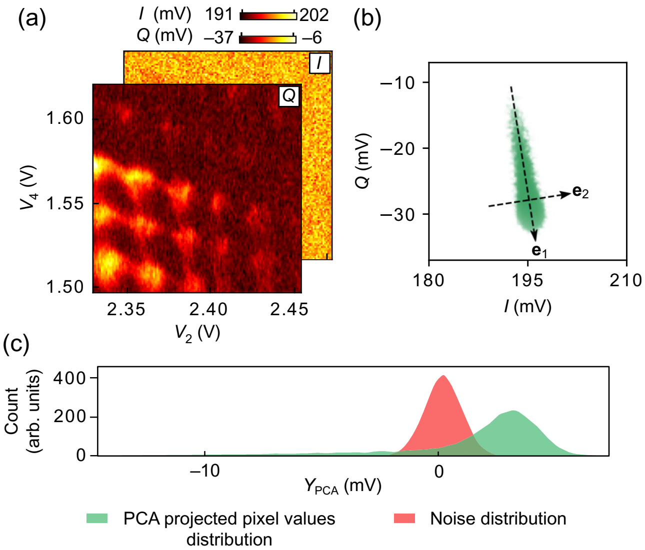

FIG. 3. (a) The demodulated in-phase (I) and out-of-phase (Q) quadratures of a 2D scan, showing double-quantum-dot features on the edge of the rf hypervolume. (b) A scatter graph of the demodulated I and Q quadratures of the 2D scans in (a). We observe two principal directions of variance. The information-bearing component can be found along e_1, while the less informative component is along e_2. (c) A histogram of the I and Q data is shown in green once projected onto e_1. For comparison, we show a histogram of premeasured noise projected similarly in red. The noise has a Gaussian distribution, while the double-dot features produce a distinctly different distribution, providing a means to distinguish them.

To test whether this projected data is dominated by noise, we then perform a two-sample Kolmogorov-Smirnov hypothesis test, as implemented in SCIPY [26,38], to compare the pixel value distribution of the projected scan against a reference noise measurement. The null hypothesis is that the two distributions are identical; therefore, the 2D scan contains just noise. The alternative hypothesis is that the distributions differ, so the scan shows quantum-dot features instead. Our critical p-value is 10^{-3}, so p-values below this critical value lead to rejecting the null hypothesis in favor of the alternative. This choice of p-value means that, on average, the null hypothesis is falsely rejected only once in every 10^3 scans.

The noise was characterized by taking ten 2D scans with all gate voltages set to their maximum value. As a way to illustrate this test, a histogram of the PCA-projected pixel values of the scan in Fig. 3(a) is overlaid on the measured reference noise distribution [Fig. 3(c)]. Quantum-dot features can be observed in Fig. 3(a), and a long-tailed distribution captures the presence of these features when compared to the noise distribution [Fig. 3(c)]. The 2D scan would thus be classified as containing features and the exploratory gate voltage ramp would terminate.

3. The score function

The role of the score function is to identify scans showing double-dot features by scoring them highly while scoring other features, such as those from single dots, poorly. Score functions used in the literature to evaluate current measurements have been based on neural networks [8,39–41], Hough transforms [7,42], custom fitting models [6], handcrafted heuristics [5], and even ray-based classification [43]. Since most of these techniques requires a high signal-to-noise ratio, we designed a score function based on the discrete-time Fourier transform of the 2D scans. This score function is naturally phase-independent and thus can evaluate both in-phase and out-of-phase scans. Owing to the properties of the Fourier transform, it is also robust against noise, allowing us to benefit from the high bandwidth of rf measurements. See Appendix E for a mathematical description of how the score function was evaluated and a discussion of the noise tolerance inherited from the Fourier transform.

The discrete-time Fourier transform of the 2D scans quantifies any periodicities present in these scans. Each periodicity results in a prominent maximum in the Fourier transform, and the more periodic the features, the higher the value of these maxima. Our score function searches the Fourier transform of 2D scans for the two maxima resulting from double-quantum-dot features. We constrain the search for these maxima to only consider periodicities consistent with two quantum dots, each coupled enough to their respective plunger gates, showing a few charge transitions over a 100-mV plunger gate sweep. In practice, if the plunger gates are V_x and V_y, we search Fourier frequencies $\nu_x, \nu_y \in [0, 12]$ arbitrary units and only considering maxima on opposite sides of $\nu_x = \nu_y$. The score function then assigns the score as the strength of the weaker of the two maxima. A scan showing single-dot features should result in just one maximum and other features in none, and thus low scores will be assigned to such scans. A comparison of double- and single-dot features with respective Fourier transforms is displayed in Figs. 4(a)–4(d).

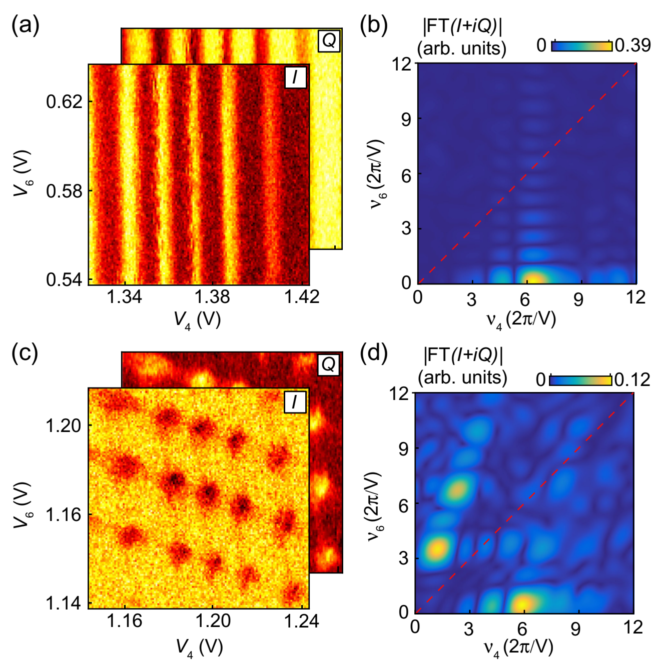

FIG. 4. (a),(b) A 2D scan showing single-dot features and corresponding time-discrete Fourier transform of the standardized I and Q data. The single-dot features show one distinct periodicity, resulting in a single strong maximum in the Fourier transform (with fringes resulting from the finite window size). (c),(d) A 2D scan shows double-dot features and the corresponding time-discrete Fourier transform of the standardized I and Q data. The double-dot features show two distinct periodicities (and associated harmonics), resulting in two strong maxima in the Fourier transform on either side of the diagonal $\nu_x = \nu_y$ marked as a dashed red line.

III. RESULTS

To evaluate the performance of our algorithm both in devices A and B, we performed 24 runs for a fixed time of an hour, which produced approximately 2×10^4 scans in total, each with an associated score. Whether each run attempted to tune configuration A or B was chosen at random, resulting in 13 attempts at tuning configuration A and 11 for configuration B. To demonstrate the success of these runs, we need first to establish that the score function is a good metric for identifying double-quantum-dot regimes and then show that the score increases as a function of tuning time and that it does so faster than more straightforward search strategies.

To quantify our score function's correlation with experts' perception of double-dot quality, we created three categories: nondouble, imperfect double, and satisfactory double dot. Two human experts classified the scans according to such labels without knowing the associated score. Figure 5(a) shows a stacked histogram of the scores, where each bar has been divided into colors based on the human experts' labels. We observe that nondouble-dot (satisfactory-quantum-dot) features reliably receive low (high) scores.

Based on Fig. 5(a), we define two score thresholds as 0.04 and 0.08. These values are chosen to produce confusion matrices reflecting the score function's performance and have no bearing on the double-quantum-dot regimes that the algorithm finds. Table I shows the confusion matrix for scans taken from both devices; confusion matrices specific to each device are presented in the Appendix. Our score function produces very few false positives even when faced with an overwhelming number of scans in which no double-quantum-dot features are present while retaining the ability to separate satisfactory from imperfect double quantum dots.

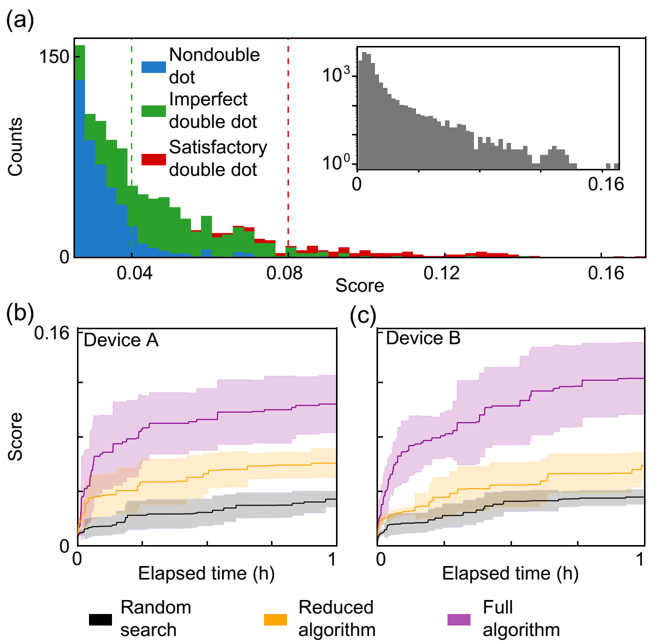

FIG. 5. (a) A histogram of the double-dot feature scores plotted on a linear scale, where the color coding of each bin indicates relative proportions of the scans judged by human labeling to be nondouble (blue), imperfect double (green) and satisfactory double dot (red). The red double-dot region lies above the blue nondouble-dot region, while the green region corresponding to satisfactory double dots lies above both the orange and the blue. For clarity, we plotted only scores above 0.025 on the linear scale due to the overwhelming number of scores below this threshold; the inset shows a histogram of all the scores on a log scale. (b),(c) The highest score found after a given tuning time for algorithms which randomly search (gray), a reduced version of the algorithm (orange), and the full algorithm (pink) in devices A and B. The curves presented are the mean of many runs to account for the statistical variation between runs. Our algorithm explores the gate voltage space more efficiently than a random search or random rays; therefore, its best score improves fastest.

We now show the improvement of the score with time. Over its run time, the algorithm explores a greater fraction of the rf hypervolume and discovers more dot features. Each newly discovered dot feature has a chance of scoring higher than anything found before; therefore, on average, the score associated with the highest-scoring features should improve over time. The purple curves in Figs. 5(b) and 5(c) show the evolution of the best score found by the algorithm as a function of run time for devices A and B, respectively. For a baseline comparison, we ran a reduced version of our algorithm, which uses the exploratory ramps but did not benefit from any of the Gaussian processes, the rf classifier (which terminated the gate voltage ramps close to the rf hypervolume), nor the subsequent random walk, shown in orange. We also ran a random search algorithm that randomly chose a coordinate in gate voltage space, set the gate voltages, and then performed a scan, shown in black.

TABLE I. Confusion matrix for configurations A and B. The values indicate the percentage of plots unanimously classified by humans as being above or below two score thresholds (0.04 and 0.08).

	Expert classification		
Configurations A, B (%)	Nondouble dot	Imperfect double dot	Satisfactory double dot
score < 0.04	96.95	0.91	0.00
$0.04 \leq$ score < 0.08	0.25	1.42	0.08
score ≥ 0.08	0.01	0.11	0.29

We find that our algorithm outperforms these more simplistic versions. This is likely because our algorithm spends a more significant fraction of its time exploring regions that have the potential to correspond to double-dot regimes.

Overall, the full algorithm found and identified 16.5 and 16.8 scans an hour on average, corresponding to double dots (satisfactory and nonideal) in devices A and B, respectively. If we restrict our attention to satisfactory double dots, the rates are 2.4 and 2.7 scans an hour. These tuning times are the fastest recorded in laterally defined quantum dots [5,35]. See Appendix G for plots of satisfactory double dots tuned by the algorithm in each hour-long run.

IV. CONCLUSION

In conclusion, we have demonstrated an algorithm for coarsely tuning double dots exclusively using rf measurements. Such a result is an essential first step toward the scalability of quantum devices. Our algorithm reliably tuned satisfactory double quantum dots in approximately 15 min, the fastest recorded time in laterally defined quantum dots, using solely rf reflectometry measurements. In creating this algorithm, we developed a robust method for distinguishing noise from rf features and proposed a score function based on the Fourier transform with significant noise tolerance.

Faster device tuning times could be achieved using a more informative Gaussian prior for the Gaussian process, particularly one which encodes knowledge of the gate architecture. Such a prior could use an electrostatic model of the device [44]. Furthermore, an additional Gaussian process and Bayesian optimization techniques could be used to choose the ramp directions.

To probe the charge states of large quantum-dot arrays, the fast 2D scans could be generalized to radial rays, as performed slowly in Refs. [43,45,46]. Along with frequency multiplexing [47], our algorithm could allow for scalable tuning and, thus, fully automatic tuning of multiple small quantum-dot arrays.

ACKNOWLEDGMENTS

We thank Nicholas Sim for providing help with the rf cavities and David Craig for his feedback on the paper. This work was supported by the Royal Society (URF-R1-191150), the EPSRC National Quantum Technology Hub in Networked Quantum Information Technology (EP/M013243/1), Quantum Technology Capital (EP/N014995/1), EPSRC Platform Grant (EP/R029229/1), the European Research Council (Grant Agreement 948932), the Scientific Service Units of IST Austria through resources provided by the nanofabrication facility, the FWF-P 30207, and FWF-I 05060 projects, and Grant No. FQXi-IAF19-01 from the Foundational Questions Institute Fund, a donor-advised fund of Silicon Valley Community Foundation.

B.v.S developed the algorithm, B.v.S. and F.F. performed the experiment, labeled and analyzed the data. The sample was fabricated by G.K., and A.B., D.C., and G.I. grew the heterostructure. N.A. supervised the experiment and conceived the project. All authors discussed the results and contributed to the writing of the paper.

Natalia Ares declares competing interests as a founder of Quantrolox, which develops machine-learning-based software for quantum device control. All other authors declare no competing financial or nonfinancial interests.

DATA AVAILABILITY

The data that support the findings of this article are openly available [48]. Embargo periods may apply.

APPENDIX A: EXPERIMENTAL SETUP

Measurements were conducted within a Triton 200 cryofree dilution refrigerator with a base temperature of 50 mK. Direct current voltages in the range of 0–4 V with 16-bit resolution were generated using an S2f DAC module with a Delft IVVI rack. The high-frequency ramps were generated using a Tektronix AWG5014C arbitrary waveform generator. As mentioned in the main text, we used bias-tees (made with standard surface-mount components in our custom printed circuit board) to combine ac and dc signals applied to gate electrodes. See Appendix C for details about the reflectometry measurements.

APPENDIX B: DEVICE ARCHITECTURE

Figure 6(a) shows an extended micrograph of our device showing the charge sensor gates on the top half of the device. The device architecture is such that up to three quantum dots and a charge sensor can be defined. For this experiment, we focused just on double-quantum-dot configurations and we kept the charge sensor gates grounded. The value of the splitter gates (V_{SL}, V_{SR}) was set to 2 V to physically separate the bottom side of the device from the top. These values are standard and validated by measurements such as those of Figs. 6(b) and 6(c). For these measurements, current flow is probed between the two pairs of ohmic contacts both at the top and bottom halves of the device [see black dash arrows in Fig. 6(a)]. In this way the gate voltage values that pinch off transport between the top and bottom half of the device can be identified [see the black dash in Figs. 6(b) and 6(c)], allowing us to solely focus on the double quantum dot.

APPENDIX C: HIGH RESOLUTION SCANS

In this appendix, we describe how fast two-dimensional scans were performed. For this task, we used a Tektronix AWG5014C arbitrary waveform generator (AWG) to feed a slow (red) and a fast (blue) sawtooth waveform to the device gates V_2, V_4, and V_6, as shown in Fig. 1(b), such that their combination would produce a raster scan in the gate voltage plane defined by V_2 and V_4 (V_4 and V_6) for configuration A (B), centered around the gate's dc voltage. Since the amplitude of the ramp determines the scan size, this is ultimately limited by different factors, including the attenuation of the cryostat lines and the Joule heating produced by this attenuation. In our setup, the total line attenuation (-28 dBm) does not pose a concern because the AWG was able to output waveform with maximum Vpp $= 5$ V. However, since we observed Joule heating of the mixing chamber for voltage scans larger than 100×100 mV, we chose this to be our scan size, thus resulting in 50-mV-amplitude waveforms as highlighted in Fig. 1(b) of the main text.

Measurements were performed by rf reflectometry, using a Zurich lock-in amplifier (UHFLI) to feed a frequency tone of 137.5 MHz to the L-matching network connected to the device ohmic and demodulate the reflected component of the signal. The resulting I and Q quadratures were finally recorded using a fast digitizer card (Alazar tech ATS9440) using an AWG marker to trigger the card acquisition such that it would be synchronized with the voltage ramps. We used an integration time per pixel of $\tau_{\text{int}} = 1\ \mu$s and a resolution of 100×100 pixels, allowing us to perform a full 2D scan within 10 ms.

As specified in the main text, a raster scan of 100×100 pixels with a waveform amplitude of 50 mV yields a resolution of 1 mV, corresponding to a 2D snapshot covering 100×100 mV in gate voltage space. This means that by varying the dc voltages on the five gate electrodes used by the algorithm by at most 50 mV, we ensure substantial overlap between consecutive snapshots along any given ray in the search space. This overlap is crucial to avoid missing the rf hypervolume. We also notice that a 50-mV step along the ray-search direction implies that each gate voltage is stepped by at most 50 mV. This is because the ray direction in gate voltage range is defined as a normalized vector whose elements (defined between 0 and 1)

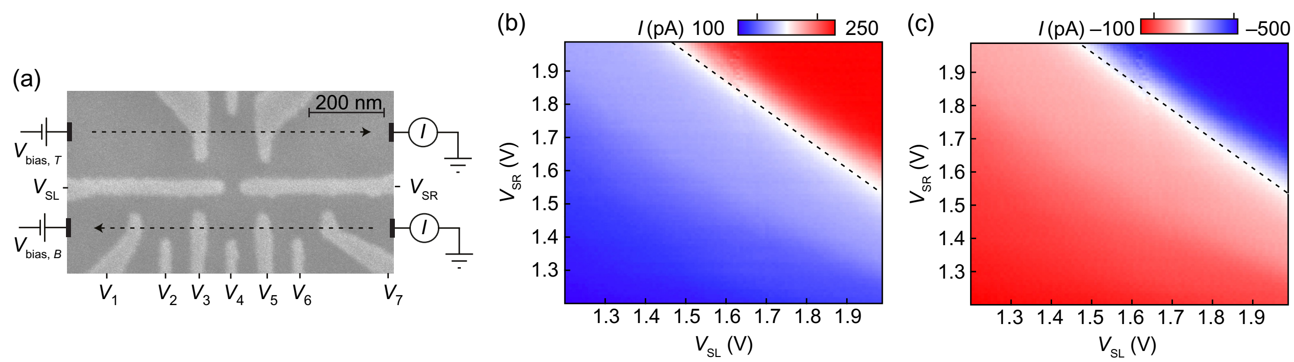

FIG. 6. (a) Extended device schematics. (b) Current I measured between pairs of source-drain contacts (along the horizontal dashed arrows), with $V_{\text{bias},T} = 1\,\text{mV}$. Black dashed lines indicate gate voltages that pinch off the transport between the bottom and top halves of the device. (c) Similar to (b), but with $V_{\text{bias},B} = -1\,\text{mV}$.

multiply the 50-mV step before these get subtracted to the preexisting dc voltage value.

1. Waveform precompensation

Although convenient to minimize low-frequency noise, the high-pass filters in the rf lines of our setup have the downside of distorting incoming waveforms by heavily attenuating the waveform's frequency components that are below the filter's cutoff frequency. Depending on the RC time of the filters, this effect can thus be significant for slow ramps and sawtooth waveforms that contain several low-frequency components in their frequency domain [49]. Nonetheless, one can easily account for the potential distortion by precompensating the incoming waveform using a function that requires just the knowledge of the filter's RC time. Because this parameter is set by the filter's design, it does not depend on the specific experiment or device being measured. To highlight this, below we briefly describe the filter's effect on a general waveform. The action of a first-order high-pass filter with a time constant τ on a signal $s(t)$ is $s_{\text{filtered}}(t) = \mathcal{F}^{-1}[\mathcal{F}[s(t)](\omega) \cdot H_{\text{HP}}(\omega)]$, where $H_{\text{HP}}(\omega) = i\omega\tau/(1 + i\omega\tau)$ and $\mathcal{F}[\cdot]$ denotes the time to frequency domain Fourier transform. To correct for this effect, we precompensated the waveforms according to $s_{\text{comp}}(t) = \mathcal{F}^{-1}[\mathcal{F}[s(t)](\omega) \cdot H_{\text{HP}}^{-1}(\omega)]$, such that the final shape reaching the device gates would be exactly $s(t)$. Precompensating the desired waveform for this filter requires only knowledge of the filter's time constant. At cryogenic temperatures, we measured the time constants to be 1.043, 1.051, and 1.025 ms for gates V_2, V_4, and V_6, respectively. Since the slow sawtooth waveform period was 10 ms, precompensation was necessary.

APPENDIX D: PROJECTION OF *I* AND *Q* DATA WITH PRINCIPAL COMPONENT ANALYSIS

When performing the fast 2D scans, we measured both the in-phase and out-of-phase quadratures. In general, both components could carry information. At the cost of recording both quadratures, PCA extracts the information-carrying signal from the noise and eliminates the need for phase adjustment. Let us consider a 2D scan with in-phase data, $\vec{I}$, and the out-of-phase data, $\vec{Q}$, where each index in these vectors corresponds to a pixel in the 2D scan. To perform blind signal separation via principal component analysis on this data, we obtained the eigenvector, $\vec{e}_1$, corresponding to the largest eigenvalue of the covariance matrix,

$$S = \begin{bmatrix} \text{cov}(\vec{I},\vec{I}) & \text{cov}(\vec{I},\vec{Q}) \\ \text{cov}(\vec{Q},\vec{I}) & \text{cov}(\vec{Q},\vec{Q}) \end{bmatrix}. \tag{D1}$$

The covariance between variables $\vec{I}$ and $\vec{Q}$ is defined as

$$\text{cov}(\vec{I},\vec{Q}) = \mathbb{E}\left[(\vec{I} - \mu_{\vec{I}})(\vec{Q} - \mu_{\vec{Q}})\right], \tag{D2}$$

where $\mathbb{E}$ is the expected value, and $\mu_{\vec{I}}$ and $\mu_{\vec{Q}}$ are the means of $\vec{I}$ and $\vec{Q}$, respectively.

We then extract the information-bearing signal, $\vec{Y}_{\text{PCA}}$, by projecting the in-phase and out-of-phase data onto this eigenvector, such that

$$\vec{Y}_{\text{PCA}} = \vec{e}_1^{\top}\mathbf{X}, \quad \text{where } \mathbf{X} = \begin{bmatrix} (\vec{I} - \bar{I}) \rightarrow \\ (\vec{Q} - \bar{Q}) \rightarrow \end{bmatrix}, \tag{D3}$$

in which $\bar{I}$ and $\bar{Q}$ denote the mean of $\vec{I}$ and $\vec{Q}$, respectively.

1. Equivalence of PCA and phase tuning

The eigenvectors and corresponding eigenvalues of the covariance matrix S represent the distribution of the dataset's variance in a new orthogonal basis composed of the eigenvectors. Each eigenvalue represents the variance of the data when projected onto its corresponding eigenvector.

The eigenvector with the largest eigenvalue, $\vec{e}_1$, is known as the first principal component. We project our data onto $\vec{e}_1$ to reduce the dimensionality of the data while capturing the majority of the variance (and therefore information) within it. This projection is given by Eq. (D3).

The eigenvector $\vec{e}_1$ is a vector in IQ space with an equation $y = mx + c$. We subtract the mean from the data so the best-fit line, which is exactly equivalent to the eigenvector with the highest corresponding eigenvalue, will also have zero mean in both dimensions, meaning its equation simplifies to $y = mx$. The gradient is therefore $m = y/x$, representing an angle of $\arctan(y/x)$. The phase of a data point in IQ space is also $\phi = \arctan(y/x)$, so the angle of the best-fit line will be at the same angle as that represented by the phase. Projecting the data onto the first principal component is therefore identical to optimally tuning the demodulation phase for a given radio-frequency measurement.

APPENDIX E: THE DISCRETE TIME FOURIER TRANSFORM SCORE FUNCTION

This section describes evaluating the discrete-time Fourier transform (DTFT) score function on the in-phase, $\vec{I}$, and out-of-phase, $\vec{Q}$, data produced by a 2D scan of resolution $N \times M$ pixels. Firstly, we combine the in-phase and out-of-phase components into one complex dataset, to obtain $\vec{Z} := \vec{I} + i\vec{Q} \in \mathbb{C}^{N\times M}$. Then we standardize these complex data $\vec{Z}$ according to $\vec{\mathcal{Z}} := (\vec{Z} - \bar{Z})/\sigma_Z$, where $\bar{Z} := \bar{I} + i\bar{Q}$ and $\sigma_Z^2 := \mathrm{var}[I] + \mathrm{var}[Q]$. The reason for standardizing the data is so that the score function reflects the quality of the double-dot features and not how well matched they are to the L-matching circuit. Next, we compute the DTFT of $\vec{\mathcal{Z}}$ according to

$$\mathrm{DTFT}[\vec{\mathcal{Z}}]_{\delta\gamma} = \frac{1}{NM}\sum_{a=1}^{N}\sum_{b=1}^{M} e^{-2\pi i(\nu_\delta^x a + \nu_\gamma^y b)}\mathcal{Z}_{ab}, \quad \text{(E1)}$$

where $\vec{\nu}^x$ and $\vec{\nu}^y$ are a high-resolution linespace of frequencies between 0 and 12, to obtain $\mathrm{DTFT}[\vec{\mathcal{Z}}] \in \mathbb{C}^{100\times 100}$. From here the score, s, is computed according to

$$s := \min\left(\max|\mathrm{FT}[\vec{\mathcal{Z}}]|_{\delta<\gamma}, \max|\mathrm{FT}[\vec{\mathcal{Z}}]|_{\delta>\gamma}\right). \quad \text{(E2)}$$

To paraphrase this formula, the score function finds the strongest periodicity presented above and below the line $\nu_x = \nu_y$ and then assigns the score to be the weaker of the two. In this manner, the score function favors double dots where each dot is coupled most strongly to its plunger gate. If just a single dot is present, there could be strong periodicity and even perhaps harmonics on one side of the line $\nu_x = \nu_y$. However, single-dot features cannot score highly without a dot coupled to the opposite plunger, as the two periodicities necessary for a high score would not be present.

TABLE II. Confusion matrix for configuration A. The values indicate the percentage (%) of plots unanimously classified by humans and that were found to be above and below two score thresholds (0.04 and 0.08).

	Expert classification		
Device A (%)	Nondouble dot	Imperfect double dot	Satisfactory double dot
score < 0.04	96.96	0.93	0.00
$0.04 \le$ score < 0.08	0.19	1.43	0.06
score ≥ 0.08	0.00	0.11	0.30

As discussed in the following section, this score function inherits considerable noise tolerance from the Fourier transform, such that the noise in the score function is suppressed compared to the noise in 2D scans by a factor of the square root of the number of pixels, NM. In our work, we used N and $M = 100$, meaning that the noise in the elements of the DTFT was suppressed by a factor of 100.

1. The discrete-time Fourier transform's noise characteristics

If $\vec{Z} \in \mathbb{C}^{N\times M}$ is a complex dataset of NM elements and $\vec{N} \in \mathbb{C}^{N\times M}$ is the corresponding Gaussian noise, where each element is complex-normally distributed such that $N_{ij} \sim \mathcal{CN}(0, \sigma_N)$ (meaning that the real and imaginary parts of elements of $\vec{N}$ are independently normally distributed with a mean of zero and variance of $\sigma_N^2/2$), then

$$\mathrm{DTFT}[\vec{Z} + \vec{N}]_{\delta\gamma} \sim \mathcal{CN}\left(\mathrm{DTFT}[\vec{Z}]_{\delta\gamma}, \sigma_N/\sqrt{NM}\right). \quad \text{(E3)}$$

Therefore, the noise is suppressed by a factor of $1/\sqrt{NM}$ in the DTFT . This can be shown by using the additive nature of the DTFT . We can write $\mathrm{DTFT}[\vec{Z} + \vec{N}]_{\delta\gamma} = \mathrm{DTFT}[\vec{Z}]_{\delta\gamma} + \mathrm{DTFT}[\vec{N}]_{\delta\gamma}$, where the time-discrete Fourier transform of the noise $\vec{N}$ is

$$\mathrm{DTFT}[\vec{N}]_{\delta\gamma} = \frac{1}{NM}\sum_{a=1}^{N}\sum_{b=1}^{M} e^{-2\pi i(\nu_\delta^x a + \nu_\gamma^y b)}N_{ab}. \quad \text{(E4)}$$

As the complex-normal distribution is circularly symmetric, the multiplication by the complex phase factor,

TABLE III. Confusion matrix for configuration B.

	Expert classification		
Device B (%)	Nondouble dot	Imperfect double dot	Satisfactory double dot
score < 0.04	96.93	0.89	0.00
$0.04 \le$ score < 0.08	0.30	1.41	0.09
score ≥ 0.08	0.01	0.10	0.27

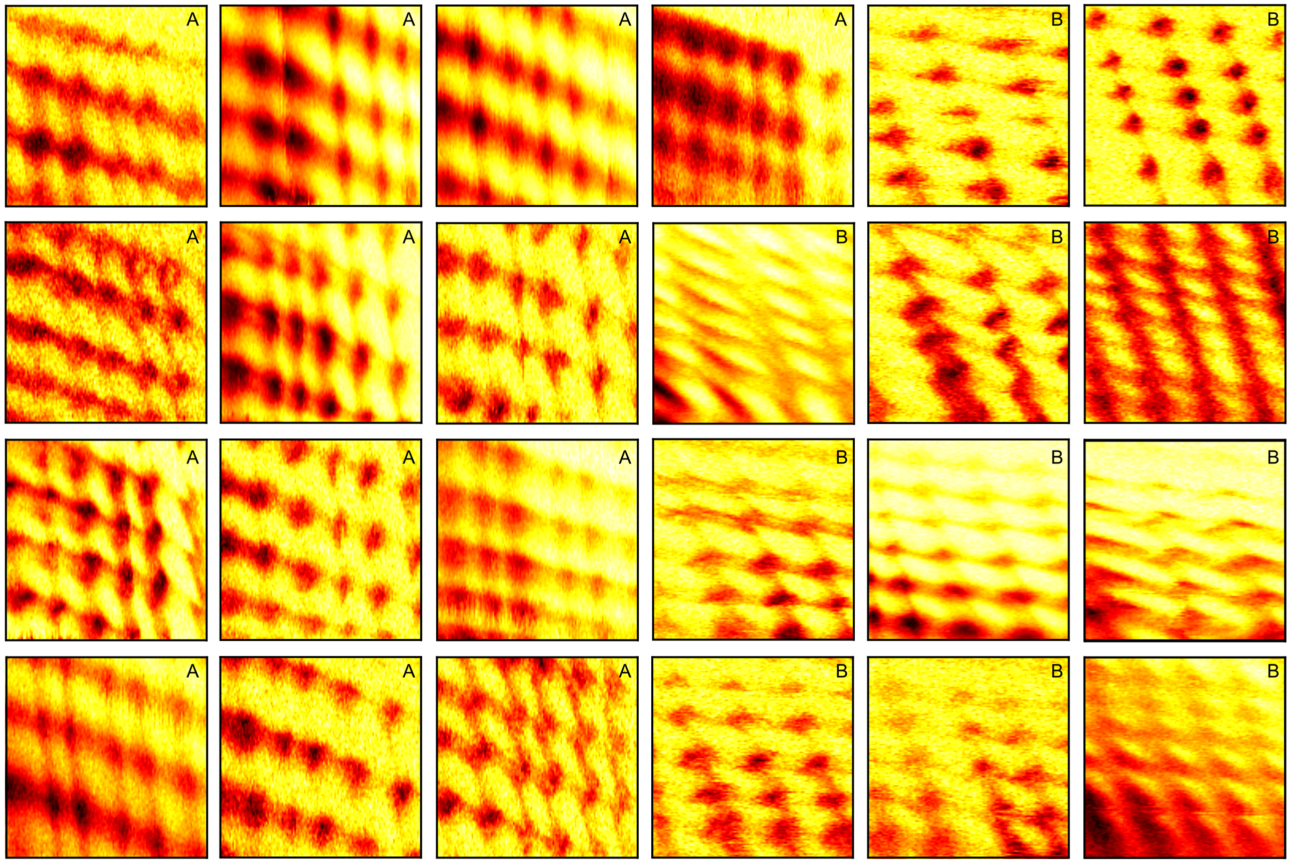

FIG. 7. The highest-scored double-dot features found by the algorithm by the end of each hour-long tuning session performed on devices A or B, labeled in the top corner. For scans taken in device A (B), the horizontal and vertical axes are gates V_2 (V_4) and V_4 (V_6) respectively; both of these gate voltages are swept over a 100 mV range. The pixel values correspond to the PCA projection described in Appendix D.

$\exp(-2\pi i(\nu_\delta^x a + \nu_\gamma^y b))$, leaves the distribution unchanged, thus $\exp(-2\pi i(\nu_\delta^x a + \nu_\gamma^y b))N_{ab} \sim \mathcal{CN}(0, \sigma_N)$, which means that $\mathrm{DTFT}[\vec{N}]_{\delta\gamma}$ can be regarded as the mean of NM samples from a complex-normal distribution. The central limit theorem predicts that this mean will be distributed as $\mathrm{DTFT}[\vec{N}]_{\delta\gamma} \sim \mathcal{CN}(0, \sigma_N/\sqrt{NM})$. As there is no uncertainty in the Fourier transform of the noiseless signal, $\vec{N}_{\delta\gamma}$ the sum of the Fourier transform of the signal and noise will be distributed according to Eq. (E3).

APPENDIX F: SEPARATED CONFUSION MATRICES FOR DEVICES A AND B

This appendix presents the confusion matrices for the score function applied to scans from devices A (Table II) and B (Table III). To evaluate the performance of the double-quantum-dot score function, two human experts labeled over 20 000 2D fast scans without knowing the scores in advance. The score thresholds thus correspond to the values that best separate the three distinct categories identified by the two human labelers. As an example (related to Table I), 96.93% of the plots that the human labelers identified to have no double-quantum-dot features received a score strictly less than 0.04. On the other hand, only 0.01% of these plots received a score greater than or equal to 0.08.

APPENDIX G: OUTCOMES FROM THE HOUR-LONG TUNING SESSIONS

The highest scoring of the double-dot features found by the algorithm in each hour-long tuning session are shown in Fig. 7.

[1] Florian Vigneau, Federico Fedele, Anasua Chatterjee, David Reilly, Ferdinand Kuemmeth, Fernando Gonzalez-Zalba, Edward Laird, and Natalia Ares, Probing quantum devices with radio-frequency reflectometry, Appl. Phys. Rev. **10**, 021305 (2023).

[2] Mark R. Hogg, Prasanna Pakkiam, Samuel K. Gorman, Andrey V. Timofeev, Yousun Chung, Gurpreet K. Gulati, Matthew G. House, and Michelle Y. Simmons, Single-shot

readout of multiple donor electron spins with a gate-based sensor, PRX Quantum **4**, 010319 (2023).

[3] Mateusz T. Madzik, Serwan Asaad, Akram Youssry, Benjamin Joecker, Kenneth M. Rudinger, Erik Nielsen, Kevin C. Young, Timothy J. Proctor, Andrew D. Baczewski, Arne Laucht, Vivien Schmitt, Fay E. Hudson, Kohei M. Itoh, Alexander M. Jakob, Brett C. Johnson, David N. Jamieson, Andrew S. Dzurak, Christopher Ferrie, Robin Blume-Kohout, and Andrea Morello, Precision tomography of a three-qubit donor quantum processor in silicon, Nature **601**, 348 (2022).

[4] G. A. Oakes *et al.*, Fast high-fidelity single-shot readout of spins in silicon using a single-electron box, Phys. Rev. X **13**, 011023 (2023).

[5] H. Moon, D. T. Lennon, J. Kirkpatrick, N. M. van Esbroeck, L. C. Camenzind, Liuqi Yu, F. Vigneau, D. M. Zumbühl, G. A. D. Briggs, M. A. Osborne, D. Sejdinovic, E. A. Laird, and N. Ares, Machine learning enables completely automatic tuning of a quantum device faster than human experts, Nat. Commun. **11**, 4161 (2020).

[6] T. A. Baart, P. T. Eendebak, C. Reichl, W. Wegscheider, and L. M. K. Vandersypen, Computer-automated tuning of semiconductor double quantum dots into the single-electron regime, Appl. Phys. Lett. **108**, 213104 (2016).

[7] A. R. Mills, M. M. Feldman, C. Monical, P. J. Lewis, K. W. Larson, A. M. Mounce, and J. R. Petta, Computer-automated tuning procedures for semiconductor quantum dot arrays, Appl. Phys. Lett. **115**, 113501 (2019).

[8] Justyna P. Zwolak, Thomas McJunkin, Sandesh S. Kalantre, J. P. Dodson, E. R. MacQuarrie, D. E. Savage, M. G. Lagally, S. N. Coppersmith, Mark A. Eriksson, and Jacob M. Taylor, Autotuning of double-dot devices *in situ* with machine learning, Phys. Rev. Appl. **13**, 034075 (2020).

[9] Damaz de Jong, Christian G. Prosko, Daan M. A. Waardenburg, Lin Han, Filip K. Malinowski, Peter Krogstrup, Leo P. Kouwenhoven, Jonne V. Koski, and Wolfgang Pfaff, Rapid microwave-only characterization and readout of quantum dots using multiplexed gigahertz-frequency resonators, Phys. Rev. Appl. **16**, 014007 (2021).

[10] Zhenyu Cai, Michael A. Fogarty, Simon Schaal, Sofia Patomäki, Simon C. Benjamin, and John J. L. Morton, A silicon surface code architecture resilient against leakage errors, Quantum **3**, 212 (2019).

[11] Ruoyu Li, Luca Petit, David P. Franke, Juan Pablo Dehollain, Jonas Helsen, Mark Steudtner, Nicole K. Thomas, Zachary R. Yoscovits, Kanwal J. Singh, Stephanie Wehner, Lieven M. K. Vandersypen, James S. Clarke, and Menno Veldhorst, A crossbar network for silicon quantum dot qubits, Sci. Adv. **4**, 3960 (2018).

[12] M. Veldhorst, H. G. J. Eenink, C. H. Yang, and A. S. Dzurak, Silicon CMOS architecture for a spin-based quantum computer, Nat. Commun. **8**, 1766 (2017).

[13] M. F. Gonzalez-Zalba, S. de Franceschi, E. Charbon, T. Meunier, M. Vinet, and A. S. Dzurak, Scaling silicon-based quantum computing using CMOS technology, Nat. Electron. **4**, 872 (2021).

[14] Arne Laucht *et al.*, Roadmap on quantum nanotechnologies, Nanotechnology **32**, 162003 (2021).

[15] A. Ruffino, T.-Y. Yang, J. Michniewicz, Y. Peng, E. Charbon, and M. F. Gonzalez-Zalba, A cryo-CMOS chip that integrates silicon quantum dots and multiplexed dispersive readout electronics, Nat. Electron. **5**, 53 (2022).

[16] A. Ruffino, Y. Peng, T.-Y. Yang, J. Michniewicz, M. F. Gonzalez-Zalba, and E. Charbon, in *2021 IEEE International Solid-State Circuits Conference (ISSCC) Digest of Technical Papers* (IEEE, San Francisco, California, USA, 2021), pp. 210–212.

[17] F. Ansaloni, H. Bohuslavskyi, F. Fedele, T. Rasmussen, B. Brovang, F. Berritta, A. Heskes, J. Li, L. Hutin, B. Venitucci, B. Bertrand, M. Vinet, Y.-M. Niquet, A. Chatterjee, and F. Kuemmeth, Gate reflectometry in dense quantum dot arrays, New J. Phys. **25**, 033023 (2023).

[18] S. Schaal, A. Rossi, V. N. Ciriano-Tejel, T.-Y. Yang, S. Barraud, J. J. L. Morton, and M. F. Gonzalez-Zalba, A CMOS dynamic random access architecture for radio-frequency readout of quantum devices, Nat. Electron. **2**, 236 (2019).

[19] Anasua Chatterjee, Paul Stevenson, Silvano De Franceschi, Andrea Morello, Nathalie P. de Leon, and Ferdinand Kuemmeth, Semiconductor qubits in practice, Nat. Rev. Phys. **3**, 157 (2021).

[20] Guido Burkard, Thaddeus D. Ladd, John M. Nichol, Andrew Pan, and Jason R. Petta, Semiconductor spin qubits, Rev. Mod. Phys. **95**, 025003 (2023).

[21] J. Stehlik, Y.-Y. Liu, C. M. Quintana, C. Eichler, T. R. Hartke, and J. R. Petta, Fast charge sensing of a cavity-coupled double quantum dot using a Josephson parametric amplifier, Phys. Rev. Appl. **4**, 014018 (2015).

[22] F. J. Schupp, F. Vigneau, Y. Wen, A. Mavalankar, J. Griffiths, G. A. C. Jones, I. Farrer, D. A. Ritchie, C. G. Smith, L. C. Camenzind, L. Yu, D. M. Zumbühl, G. A. D. Briggs, N. Ares, and E. A. Laird, Sensitive radiofrequency readout of quantum dots using an ultra-low-noise SQUID amplifier, J. Appl. Phys. **127**, 244503 (2020).

[23] Ian T. Jolliffe and Jorge Cadima, Principal component analysis: A review and recent developments, Philos. Trans. R. Soc. A: Math. Phys. Eng. Sci. **374**, 20150202 (2016).

[24] Madhab Pal, Rajib Roy, Joyanta Basu, and Milton S. Bepari, in *2013 International Conference Oriental COCOSDA held jointly with 2013 Conference on Asian Spoken Language Research and Evaluation (O-COCOSDA/CASLRE)* (IEEE, Gurgaon, India, 2013), pp. 1–5.

[25] *Handbook of Blind Source Separation*, edited by P. Comon and C. Jutten (Academic Press, Oxford, 2010), pp. xxiii–xxiv, https://www.sciencedirect.com/book/9780123747266/handbook-of-blind-source-separation.

[26] J. L. Hodges, The significance probability of the Smirnov two-sample test, Ark. Mat. **3**, 469 (1958).

[27] Giordano Scappucci, Christoph Kloeffel, Floris A. Zwanenburg, Daniel Loss, Maksym Myronov, Jian-Jun Zhang, Silvano De Franceschi, Georgios Katsaros, and Menno Veldhorst, The germanium quantum information route, Nat. Rev. Mater. **6**, 926 (2021).

[28] Hannes Watzinger, Josip Kukučka, Lada Vukušić, Fei Gao, Ting Wang, Friedrich Schäffler, Jian-Jun Zhang, and Georgios Katsaros, A germanium hole spin qubit, Nat. Commun. **9**, 3902 (2018).

[29] Daniel Jirovec, Andrea Hofmann, Andrea Ballabio, Philipp M. Mutter, Giulio Tavani, Marc Botifoll, Alessandro Crippa, Josip Kukucka, Oliver Sagi, Frederico Martins, Jaime Saez-Mollejo, Ivan Prieto, Maksim Borovkov, Jordi

Arbiol, Daniel Chrastina, Giovanni Isella, and Georgios Katsaros, A singlet-triplet hole spin qubit in planar Ge, Nat. Mater. **20**, 1106 (2021).

[30] N. W. Hendrickx, D. P. Franke, A. Sammak, G. Scappucci, and M. Veldhorst, Fast two-qubit logic with holes in germanium, Nature **577**, 487 (2020).

[31] Nico W. Hendrickx, William I. L. Lawrie, Maximilian Russ, Floor van Riggelen, Sander L. de Snoo, Raymond N. Schouten, Amir Sammak, Giordano Scappucci, and Menno Veldhorst, A four-qubit germanium quantum processor, Nature **591**, 580 (2021).

[32] Ke Wang, Gang Xu, Fei Gao, He Liu, Rong-Long Ma, Xin Zhang, Zhanning Wang, Gang Cao, Ting Wang, Jian-Jun Zhang, Dimitrie Culcer, Xuedong Hu, Hong-Wen Jiang, Hai-Ou Li, Guang-Can Guo, and Guo-Ping Guo, Ultrafast coherent control of a hole spin qubit in a germanium quantum dot, Nat. Commun. **13**, 206 (2022).

[33] N. Ares, F. J. Schupp, A. Mavalankar, G. Rogers, J. Griffiths, G. A. C. Jones, I. Farrer, D. A. Ritchie, C. G. Smith, A. Cottet, *et al*., Sensitive radio-frequency measurements of a quantum dot by tuning to perfect impedance matching, Phys. Rev. Appl. **5**, 034011 (2016).

[34] K. D. Petersson, C. G. Smith, D. Anderson, P. Atkinson, G. A. C. Jones, and D. A. Ritchie, Charge and spin state readout of a double quantum dot coupled to a resonator, Nano Lett. **10**, 2789 (2010).

[35] B. Severin, Dominic T. Lennon, Leon C. Camenzind, Florian Vigneau, F. Fedele, D. Jirovec, A. Ballabio, D. Chrastina, G. Isella, M. de Kruijf, *et al*., Cross-architecture tuning of silicon and SiGe-based quantum devices using machine learning, Sci. Rep. **14**, 17281 (2024).

[36] Fabian Pedregosa, Gael Varoquaux, Alexandre Gramfort, Vincent Michel, Bertrand Thirion, Olivier Grisel, Mathieu Blondel, Peter Prettenhofer, Ron Weiss, Vincent Dubourg, Jake VanderPlas, Alexandre Passos, David Cournapeau, Matthieu Brucher, Marius Perrot, Édouard Duchesnay, Scikit-learn: Machine learning in Python, J. Mach. Learn. Res. **12**, 2825- (2011).

[37] Alaa Tharwat, Independent component analysis: An introduction, Appl. Comput. Inf. **17**, 222 (2021).

[38] Pauli Virtanen, and SciPy 1.0 Contributors *et al*., SciPy 1.0: Fundamental algorithms for scientific computing in Python, Nat. Methods **17**, 261 (2020).

[39] Sandesh S. Kalantre, Justyna P. Zwolak, Stephen Ragole, Xingyao Wu, Neil M. Zimmerman, Michael D. Stewart, and Jacob M. Taylor, Machine learning techniques for state recognition and auto-tuning in quantum dots, npj Quantum Inf. **5**, 1 (2019).

[40] Joshua Ziegler, Thomas McJunkin, E. S. Joseph, Sandesh S. Kalantre, Benjamin Harpt, D. E. Savage, M. G. Lagally, M. A. Eriksson, Jacob M. Taylor, and Justyna P. Zwolak, Toward robust autotuning of noisy quantum dot devices, Phys. Rev. Appl. **17**, 024069 (2022).

[41] Anton Zubchenko, Danielle Middlebrooks, Torbjørn Rasmussen, Lara Lausen, Ferdinand Kuemmeth, Anasua Chatterjee, and Justyna P. Zwolak, Autonomous bootstrapping of quantum dot devices, Phys. Rev. Appl. **23**, 014072 (2025).

[42] M. Lapointe-Major, O. Germain, J. Camirand Lemyre, D. Lachance-Quirion, S. Rochette, F. Camirand Lemyre, and M. Pioro-Ladrière, Algorithm for automated tuning of a quantum dot into the single-electron regime, Phys. Rev. B **102**, 085301 (2020).

[43] Justyna P. Zwolak, Thomas McJunkin, Sandesh S. Kalantre, Samuel F. Neyens, E. R. MacQuarrie, Mark A. Eriksson, and Jacob M. Taylor, Ray-based framework for state identification in quantum dot devices, PRX Quantum **2**, 020335 (2021).

[44] David L. Craig, H. Moon, Federico Fedele, Dominic T. Lennon, B. Van Straaten, Florian Vigneau, Leon C. Camenzind, Dominik M. Zumbühl, G. Andrew D. Briggs, Michael A. Osborne, *et al*., Bridging the reality gap in quantum devices with physics-aware machine learning, Phys. Rev. X **14**, 011001 (2024).

[45] Anasua Chatterjee, Fabio Ansaloni, Torbjørn Rasmussen, Bertram Brovang, Federico Fedele, Heorhii Bohuslavskyi, Oswin Krause, and Ferdinand Kuemmeth, Autonomous estimation of high-dimensional coulomb diamonds from sparse measurements, Phys. Rev. Appl. **18**, 064040 (2022).

[46] Oswin Krause and Anasua Chatterjee Ferdinand Kuemmeth Evert van Nieuwenburg, Learning coulomb diamonds in large quantum dot arrays, Scipost Phys. **13**, 084 (2022).

[47] J. M. Hornibrook, J. I. Colless, A. C. Mahoney, X. G. Croot, S. Blanvillain, H. Lu, A. C. Gossard, and D. J. Reilly, Frequency multiplexing for readout of spin qubits, Appl. Phys. Lett. **104**, 103108 (2014).

[48] Barnaby van Straaten, Federico Fedele, Florian Vigneau, Joseph Hickie, Daniel Jirovec, Daniel Chrastina, Giovanni Isella, and Natalia Ares, All rf-based tuning algorithm for quantum devices using machine learning, Zenodo dataset, 2025, https://doi.org/10.5281/zenodo.17352654.

[49] F. Fedele, Spin interactions within a two-dimensional array of GaAs double dots, Ph.D. thesis, Niels Bohr Institute, 2020, available online at https://nbi.ku.dk/english/theses/phd-theses/federico-fedele/.